ACS Catalysis

pubs.acs.org/acscatalysis
Research Article

Fe−Sn−N−C Catalysts: Advancing Oxygen Reduction Reaction Performance

Julia G. Buschermöhle,* Julia Müller-Hülstede, Henrike Schmies, Dana Schonvogel, Tanja Zierdt, Rene Lucka, Franz Renz, Peter Wagner, and Michael Wark

Cite This: ACS Catal. 2025, 15, 4477−4488
Read Online

ACCESS | Metrics & More | Article Recommendations | Supporting Information

ABSTRACT: High-temperature proton exchange membrane fuel cells (HT-PEMFCs) typically rely on platinum-based catalysts, which require high loadings due to Pt deactivation by phosphates from the phosphoric acid-doped membrane. As alternative catalysts for the oxygen reduction reaction, metal−nitrogen-carbons (M−N−Cs) are promising due to their high intrinsic activity and tolerance to phosphates. However, low volumetric activity compared to Pt nanoparticles on carbon blacks (Pt/C) and insufficient stability limit their applicability. In order to enhance the stability and activity of Fe−N−Cs, this study investigates the incorporation of tin as a second metal, resulting in Fe−Sn−N−Cs, prepared by a metal−organic framework (MOF)-based approach. Stable and highly active catalysts with total mass activities of 8.2 A g^{-1} (Fe−Sn−N−C (1:1)) and 19.3 A g^{-1} (Fe−Sn−N−C (1:0.3)) in 0.5 mol L^{-1} H_3PO_4, drastically exceeding those of the commercial Fe−N−C catalyst PMF-014401 (Pajarito-Powder, 4.8 A g^{-1}), are obtained by a synthesis without the need for subsequent purification steps. A stress test under harsh conditions (0.6−1.0 V_{RHE}, 10,000 cycles, O_2-saturated electrolyte) ascertains stability-enhancing effects of tin, highlighting an increase in stability in conjunction with the tin content. These results provide a valuable contribution to the development of cost-effective HT-PEMFCs by significantly enhancing the catalytic activity of platinum group metal-free catalysts.

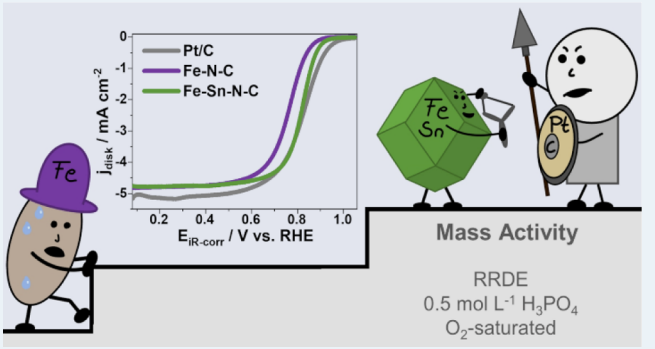

KEYWORDS: *PEM fuel cells, oxygen reduction reaction, non-PGM catalysts, metal organic frameworks, multimetallic catalysts, M−N−C, rotating ring disc electrode*

1. INTRODUCTION

In the search for renewable energy sources, the utilization of green hydrogen in fuel cells offers promising avenues for power generation in automotive, stationary, and portable applications.[1] Therefore, fuel cells are viable candidates to drive the energy transition and reduce dependency on fossil fuels.[2] Proton exchange membrane fuel cells (PEMFCs) are a type of fuel cell that employs a polymer membrane to mediate proton exchange between the anode and cathode. In PEMFCs, electrocatalysts facilitate the conversion of hydrogen and oxygen into water, releasing electrical energy and heat in the process.[3] Low-temperature (LT)-PEMFCs, which are operated at 60−80 °C, use hydrated gases to ensure optimum proton conduction. However, the typical Pt-based catalysts of LT-PEMFCs are susceptible to contamination with impurities, including CO and H_2S, which are present in reformed hydrogen derived from natural gas or methanol.[3−5] This poisoning can be largely avoided in high-temperature (HT)-PEMFCs by increasing the operating temperature to 120−180 °C. As a result, the utilization of reformate gases in volume-critical applications is possible.[6,7] Moreover, HT-PEMFCs predict potential applications in the aviation industry, as they allow highly efficient heat rejection compared to LT-PEMFCs. Additionally, the necessity for humidity management is negated, thereby eliminating the need for optimization of pressure and humidity due to the fluctuations that occur during flight.[8−10] Despite their promising potential, the widespread adoption of HT-PEMFCs faces critical challenges, primarily associated with the catalysts used in the oxygen reduction reaction (ORR) at the cathode, which play a key role in the electrochemical conversion of hydrogen to electricity, heat, and water. The development of efficient and cost-effective ORR catalysts therefore has become a focal point of fuel cell technology research. While platinum group metals (PGM)-based catalysts have historically dominated the industry due to

Received: October 15, 2024
Revised: February 4, 2025
Accepted: February 6, 2025
Published: March 2, 2025

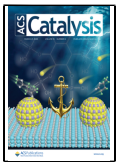

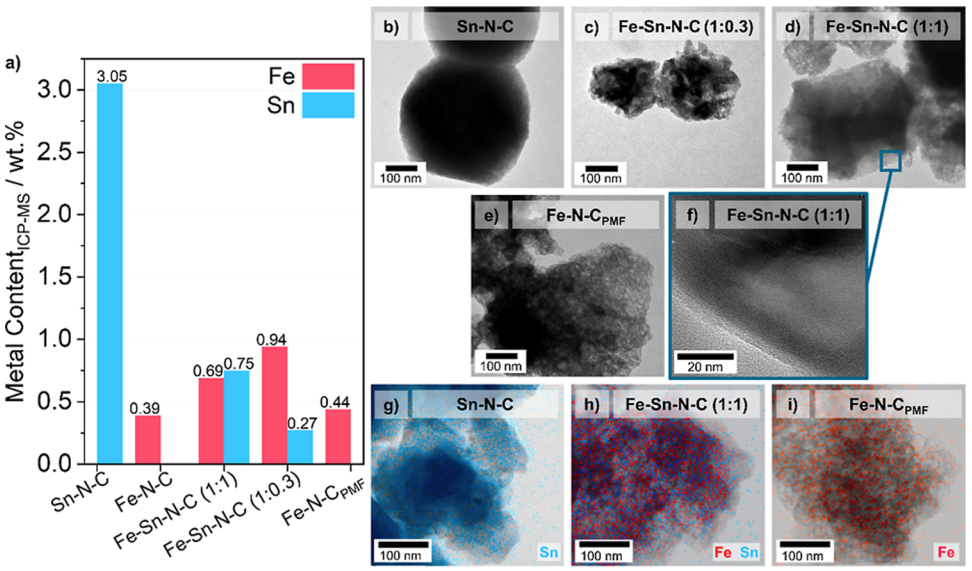

Figure 1. (a) Fe and Sn contents from ICP−MS, (b−e) transmission electron microscopy (TEM) images of the catalysts, (f) HR-TEM image of the Fe−Sn−N−C (1:1), and (g−i) STEM/EDS mappings of Sn and Fe.

their high activity, they are hampered by factors such as limited availability, high cost, and deactivation due to phosphate adsorption from the phosphoric acid-doped membrane, leading to increased demand for high loadings.[11,12] In HT-PEMFCs, the platinum loading per electrode is up to 1 mg_{Pt} cm^{-2}. In contrast, LT-PEMFCs allow for less than 0.3 mg_{Pt} cm^{-2} per electrode.[13−15]

In response to these challenges, metal−nitrogen−carbon (M−N−C) catalysts have emerged as a promising alternative to PGM catalysts. These catalysts consist of a partially graphitic carbon framework embedded with transition metal−nitrogen ($M-N_x$) sites.[16] M−N−C catalysts offer several advantages, including resistance to phosphate poisoning, a common issue encountered with Pt nanoparticles on carbon blacks (Pt/C).[17] However, challenges persist with M−N−C catalysts, including lower volumetric activities compared to Pt/Cs (at 0.8 V_{RHE} 230 A cm^{-3} for Fe−N−Cs[18] and 1300 A cm^{-3} for Pt/C[19]) and inadequate stabilities (activity losses up to 47 % during the first 100 h of PEMFC operation), which undermine their practical application.[20−22] Overcoming these challenges is therefore critical to unlock the full potential of M−N−C catalysts in PEMFC.

Nevertheless, the preparation of M−N−Cs may prove to be as challenging as their application, given the potential for complications during the synthesis route, which is typically complex and includes numerous steps.[23] The metal−organic framework (MOF)-based synthesis route has been established due to its streamlined process, which eliminates any concern of unwanted metallic particle formation.[24−26] Furthermore, the manufacturing process is not complicated by the use of acid leaching or template removal, which are costly, potentially unsafe, and therefore limit scalability.[27] Imidazolate-MOFs offer high nitrogen contents and, due to their porous nature, provide a structured pore system with a large surface area, making them ideal precursors for catalyst development.

Furthermore, the incorporation of a second metal could lead to promising synergistic effects. Consequently, not only Pt-alloys but also M−M−N−Cs have emerged as high-performance catalysts for ORR.[28,29] Currently, Fe−Co−N−Cs, Fe−Sn−N−Cs, Fe−Ni−N−Cs, and a number of other combinations have been investigated yet.[24,30,31] With M−M−N−Cs, a distinction is made between bimetallic single atom catalysts (SACs), where two distinct metals are incorporated but are not in atomic vicinity to each other, and dual atom catalysts (DACs), which are defined by the colocation of the metal centers in close proximity.[28,32] It is proposed that DACs exhibit synergistic effects, such as an electronic effect between the metals.[32] Tin can either benefit the reaction by acting as a redox-active participant or indirectly influence the electronic environment of redox-active Fe sites. Nevertheless, despite the absence of a direct bond in bimetallic SACs, beneficial effects resulting from the presence of a second metal can still occur. The group of Strasser achieved promising mass activities (MAs) of up to 4.8 A g^{-1} (0.8 V_{RHE}, 0.1 mol L^{-1} $HClO_4$) with a carbon support-based Fe−Sn−N−C. However, no evidence of atomic proximity between Fe and Sn could be identified, suggesting the formation of a bimetallic SAC with beneficial effects of the Sn on the Fe incorporation, resulting in a higher number of active Fe sites.[31] Many of the prior studies on Fe−M−N−Cs have predominantly concentrated on a single metal ratio (typically 1:1), making it challenging to identify trends.[24,31] Moreover, the majority of these studies have been conducted with 0.1 mol L^{-1} $HClO_4$ or 0.5 mol L^{-1} H_2SO_4 as the electrolyte,[24,31,33−35] whereas we have tested our catalysts in 0.5 mol L^{-1} H_3PO_4, which more closely resembles the conditions that would be found in an HT-PEMFC, which has a much more distinct challenge with high Pt loadings than the LT-PEM type. For comparison, the same tests were also carried out in 0.1 mol L^{-1} $HClO_4$.

Also, despite the crucial importance of catalyst stability in ORR, it is notable that not all studies have employed an accelerated stress test (AST), or that ASTs have been conducted in a N_2 atmosphere, which is claimed to be unsuitable for accurately testing the stability for later applications in fuel cells.[31,35]

With regard to the selection of the second metal, tin offers a significant advantage in comparison to other metals, including iron and cobalt, due to its inability to catalyze the production of reactive oxygen species (ROS). This characteristic may

https://doi.org/10.1021/acscatal.4c06338
ACS Catal. 2025, 15, 4477−4488

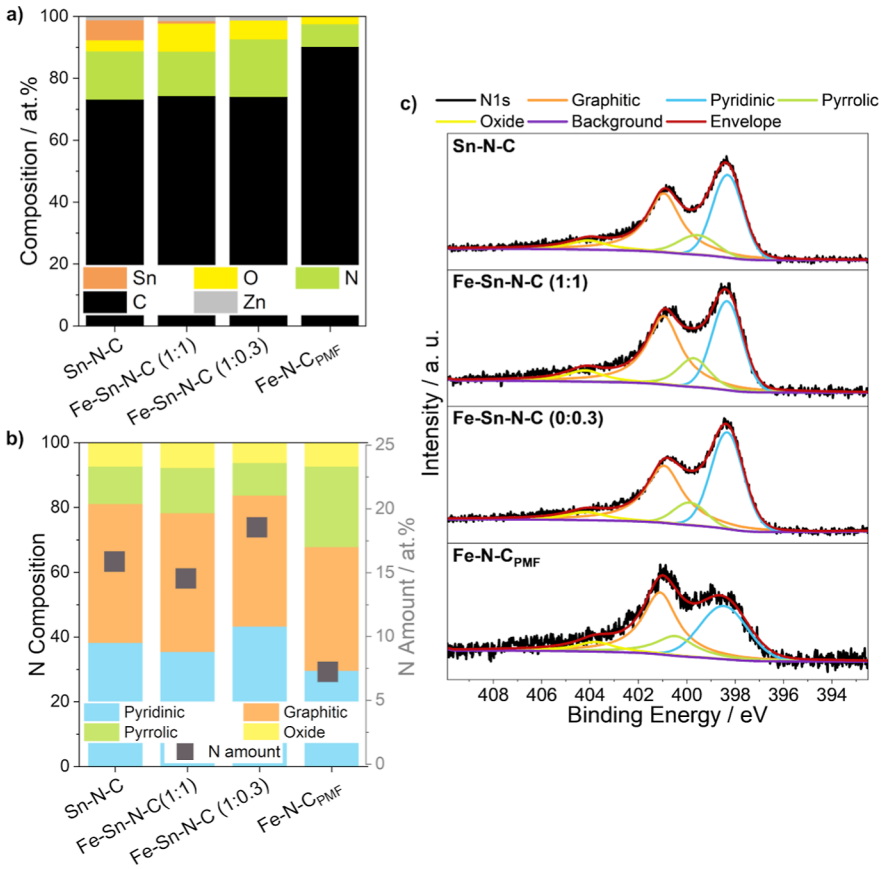

Figure 2. (a) Elemental composition of the catalysts determined from the high-resolution XP-spectra (Supporting Information Figures S4 and S5), (b) percentages of nitrogen species and total N amount determined from the N 1s spectra, and (c) N 1s high-resolution XP-spectra of the catalysts with peak fittings.

enhance the stability of the material, as ROS accelerate catalyst degradation.[36]

Herein, we report the synthesis of ZIF-8-based Fe and Sn-containing catalysts in different ratios to investigate the influence of metal ratios on catalytic activity and stability toward ORR. We use a synthetic approach that avoids the need for subsequent purification steps, thereby streamlining the synthesis process. Furthermore, an AST under harsh conditions (0.6−1.0 V_{RHE}, 10,000 cycles, O_2 saturated electrolyte) is applied to evaluate the stability of the catalysts. In order to gain a deeper understanding of the catalyst structure and the complex degradation mechanism, a series of physical analyses were conducted, which were complemented by a comprehensive degradation analysis. This work highlights not only the potential of ZIF-based catalysts for the ORR but also the potential of second metal doping for ORR catalysis.

2. RESULTS AND DISCUSSION

2.1. Catalyst Morphology and Structure. Four catalysts were investigated in this study: Sn−N−C, Fe−N−C, Fe−Sn−N−C (1:1), and Fe−Sn−N−C (1:0.3). The nomenclature of these catalysts is based on the actual metal weight ratios determined by inductively coupled plasma mass spectrometry (ICP−MS, Figure 1a and Supporting Information Table S1). The selection criteria for the doping ratios (Fe/Sn) are discussed in the Supporting Information.

The preparation of the catalysts involves doping ZIF-8 with iron and tin salts followed by pyrolysis (Supporting Information Figure S1). A pyrolysis temperature of 1000 °C was determined to be optimal for the M−M−N−C synthesis as a trade-off between activity and an acceptable residual amount of ORR inactive zinc from the ZIF-8, as shown in the Supporting Information in Table S2. The zinc content of the catalyst was found to be within a range of 2.9−3.9 wt.% (from ICP−MS) in the present study, which is lower than in other ZIF-based catalysts,[17,25] in particular without an acid leaching step involved. Although the removal of zinc is desirable, given that it is not ORR active, no additional treatment method is known to reduce the zinc content further.[17,37] It is possible that the remaining zinc is present in a molecular structure, which could result in an increase in the boiling point and, consequently, only partial evaporation. A commercial Fe−N−C catalyst (PMF-014401, Pajarito Powder), denoted as Fe−N−C_{PMF}, was used as a benchmark for comparative evaluation to assess the structures and performances.

First, the metal contents in wt.% were determined by ICP−MS (Figure 1a). The Fe−N−C_{PMF} shows the lowest iron content with 0.44 wt.%, while Fe−Sn−N−C (1:1) and Fe−Sn−N−C (1:0.3) display slightly higher iron levels with 0.69 and 0.95 wt.%, respectively. Despite the same amount of iron doping, as shown in Table S1, the iron contents of the catalysts differ considerably. Since ZIF-8 is first doped with tin, potential attachment sites could already be occupied, thus limiting additional doping with iron. Tin contents are in accordance with the applied doping amount with 3.05 wt.% for Sn−N−C, 0.75 wt.% for Fe−Sn−N−C (1:1), and 0.27 wt.% for Fe−Sn−N−C (1:0.3).

https://doi.org/10.1021/acscatal.4c06338
ACS Catal. 2025, 15, 4477−4488

Next, the morphology was analyzed by TEM, and the elemental distribution was analyzed by energy dispersive X-ray spectroscopy (EDS). The TEM images in Figure 1b−d and the HR-TEM image in Figure 1f show that the distinctive dodecahedral structure of ZIF-8, characterized by smooth and sharp edges and the absence of visible pores or irregularities (see Supporting Information Figure S2), has been significantly deconstructed by pyrolysis. The pyrolysis process at 1000 °C resulted in the partial evaporation of zinc (boiling point of 907 °C[38]) from the structure, while the M−N_x centers were incorporated into the resulting defects in the carbon matrix. The morphology has undergone a significant change, appearing more porous, and a heterogeneous, coarse-meshed carbon structure has formed. Nevertheless, after pyrolysis, the basic dodecahedral shape is still recognizable. The carbon matrix is more extensively decomposed in materials with a lower Sn content, indicating that tin increases the structural stability. Furthermore, no unwanted metallic clusters were observed, which was also confirmed by powder X-ray diffraction (PXRD, Supporting Information Figure S3) and EDS (Figure 1g−i). The absence of metal agglomerates is a favorable characteristic since inactive metal clusters have been reported with other synthesis methods for bimetallic M−M−N−Cs, both for ZIF-based and carrier-based synthesis approaches.[33,39] The morphology of the commercial Fe−N−C_{PMF} (Figure 1e,i) differs from the ZIF-based catalysts, which can be attributed to the different synthesis method. In particular, the pore structure of the carbon material is more heterogeneous in the commercial catalyst.

For further analysis of the elemental composition, a survey spectrum and high-resolution spectra of Fe, Sn, N, C, Zn, and O were recorded by X-ray photoelectron spectroscopy (XPS) (see Supporting Information Figures S4 and S5). The data was subjected to fitting; however, this was not performed on the Fe2P spectrum due to the insufficient Fe content, which precluded an appropriate fit. The expected peak positions of the configurations of iron were indicated by lines in Figure S5b. The elemental composition as seen in Figure 2a displays carbon to be the largest fraction in all catalysts, with contents of about 74 at.% for the ZIF-based catalyst and around 90 at.% for the Fe−N−C_{PMF}. Aside from small Zn residues (1.3−1.5 at. %) in the ZIF-based samples, significantly higher portions of *N* species (12−19 at.%) compared to Fe−N−C_{PMF} (7 at.%) are found.

The catalysts in this study show significantly higher N amounts compared to literature values, which are mostly around 5 at.%.[31,39−42] Due to the high N content in the prepared catalysts, a higher number of M−N_x centers and N functionalities can be expected, which can increase the activity for ORR. However, the exact type of N functionalities is important since the 4-electron-based ORR mechanism in acidic electrolyte occurs only via M−N_x centers.[43] In the presence of primarily metal-free N functionalities like pyridinic, pyrrolic, or graphitic nitrogen, the selectivity toward the 4-electron pathway decreases, and more unwanted hydrogen peroxide is formed.[44] For identification of the N species, the high-resolution N 1s spectra are shown in Figure 2c with corresponding ratios of species in Figure 2b. The fitting was performed with four N species constant, according to comparable components from the literature.[16,45−47] The four peaks correspond to pyridinic (398.5 eV), pyrrolic (400.3 eV), graphitic (401.1 eV), and oxidic nitrogen (403.5 eV).

The fractions of pyridinic and pyrrolic N species, which include the incorporated M−N_x sites, are 35−43 % and 12−14 %, respectively, in the ZIF-based catalysts, while proportions of 30 % and 25 % were found in Fe−N−C_{PMF}. Although pyridinic $FeN_4(C_{10})$ and pyrrolic $FeN_4(C_{12})$ functionalities are initially similarly active for the ORR, inactive iron oxide cluster formation from $FeN_4(C_{12})$ functionalities during operation in the PEMFC has been observed in the literature.[48] Furthermore, metal-free pyridinic functionalities are preferred over the pyrrolic ones, as they are capable of further reducing the formed H_2O_2 to H_2O.[49] However, it should also be noted that the remaining zinc can form pyridinic nitrogen compounds, which could increase the amount of this type of nitrogen while being inactive.[17] In all catalysts, oxidic nitrogen (4.7−7.7 %), which is inactive for the ORR,[50] has the lowest proportion of total nitrogen species.

The character of the structural components forming the active sites was investigated by ^{57}Fe−Mössbauer spectroscopy (Figure 3 and Supporting Information Figure S6) at room

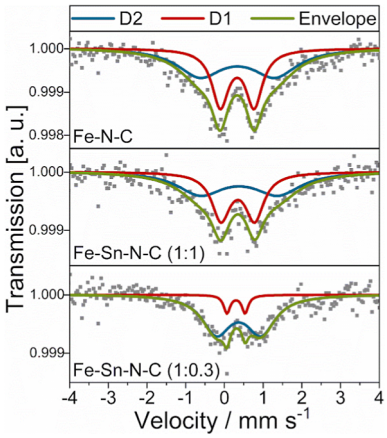

Figure 3. ^{57}Fe−Mössbauer spectra of the ZIF-based catalysts measured at room temperature with fits of D1 and D2.

temperature. To provide a substantiated conclusion, the analogous prepared Fe−N−C was measured for comparison to the Fe−Sn−N−Cs. The low metal amounts (see Figure 1) resulted in a low signal-to-noise ratio, which made it challenging to draw a well-founded conclusion regarding the SAC or DAC character of the catalysts. Two doublets (D1 and D2) were used for the fittings (Figure 3, Supporting Information Figure S6 and Table S3).[51−55] The presence of D1, attributed to low-spin Fe(II)−N_4 sites, is reported to be highly active in the ORR,[51,53,55] with ratios of 44 % and 46 % for Fe−N−C and Fe−Sn−N−C (1:1) and 10 % for Fe−Sn−N−C (1:0.3), respectively, providing a good basis for high activity. High proportions of D2, assigned to high-spin Fe(II)−N_4 sites, were also detected in all catalysts, with similar ratios for Fe−N−C and Fe−Sn−N−C (1:1) of 57 % and 54 %, respectively, and a high ratio of 90 % for Fe−Sn−N−C (1:0.3) (Supporting Information Table S3). The D2 Fe(II)−N_4 sites are proposed to enhance the catalytic activity,[56] indicating a particularly high activity for Fe−Sn−N−C (1:0.3). Moreover, in agreement with the XRD and TEM results, no metallic iron was detected.

Given that the isomer shifts and quadrupole splittings are in similar ranges for Fe−N−C and the Fe−Sn−N−Cs (Figure 3), indicating comparable coordination environments, and that

https://doi.org/10.1021/acscatal.4c06338
ACS Catal. 2025, 15, 4477−4488

there is no significant difference between the Mössbauer parameters and those reported in the literature, it can be assumed that there is no direct binding of Fe and Sn. Nevertheless, the possibility of a certain proximity of the metal centers, which could result in beneficial effects induced by Sn, cannot be excluded. In order to enhance the quality of the Mössbauer data, it is advised that future measurements should be conducted at low temperatures for a sufficiently extended duration and with a larger quantity of sample, in an effort to more accurately capture the complexity of the iron sites.

The prepared catalysts are characterized by the absence of metallic agglomerates and the presence of atomically dispersed metals, indicating that these metallic components are integrated into the catalyst structure at an atomic level.[28,31] In addition, they contain high levels of pyridinic and pyrrolic nitrogen and high levels of ORR active iron species, which are indicative of high activity and performance.

2.2. Electrochemical ORR Activity and Stability in Acidic Electrolyte. For the evaluation of ORR activity, selectivity, and stability in acidic electrolytes, rotating ring disc electrode (RRDE) measurements were performed at room temperature. The choice of phosphoric acid as an electrolyte is based on its role in the HT-PEMFC application later. Moreover, given the vulnerability of Pt/C due to phosphate poisoning, it is necessary to assess the tolerance of the M−N−C catalysts against phosphates.

First, the MAs for the ORR in 0.5 mol L^{-1} H_3PO_4 at 0.8 V_{RHE} were determined (Figure 4). In addition to the Sn−N−C and the two Fe−Sn−N−Cs, the analogous synthesized Fe−N−C was measured as well as the commercial catalysts from Pajarito Powder and Tanaka, Fe−N−C_{PMF} and Pt/C_{Tanaka}, for comparison. In the ORR curves (Figure 4a), there are notable differences between the diffusion-limited areas visible, which appear to be approximately between 0.0 and 0.4 V_{RHE}. The current values decrease in the following order: Sn−N−C > Fe−N−C > Fe−Sn−N−C (1:1) > Fe−Sn−N−C (1:0.3) > Fe−N−C_{PMF} > Pt/C_{Tanaka}. This may be attributed to the presence of more active sites, higher electrochemical surface areas, and also the nature of these sites. Additionally, the morphology of the catalyst inks may have an impact, as larger particle sizes were observed to correlate with less negative values for the limited current.[57,58] The sizes of the ZIF particles were found to be within the same range for the catalysts (Ø 200−300 nm); however, there is a possibility of a discrepancy in ink dispersion, resulting in variations in surface roughness on the disc.

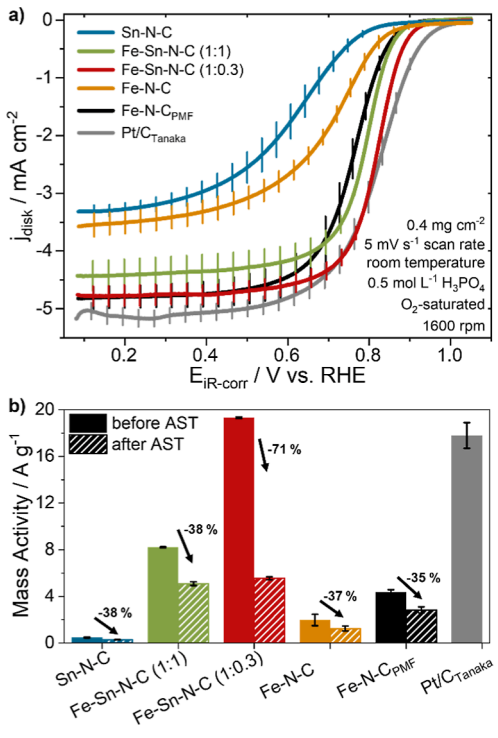

Figure 4. (a) Anodic scans of the ORR polarization curves at 1600 rpm (O_2 saturated 0.5 mol L^{-1} H_3PO_4, 400 $\mu g_{catalyst}$ cm^{-2}) with a scan rate of 5 mV s^{-1} with indicated standard deviation of 3 measurements and (b) MAs determined from ORR curves at 0.8 V_{RHE} before and after the AST with indicated standard deviation.

The MA values were extracted from the ORR curves at 0.8 V_{RHE} (Figure 4a,b). Fe−Sn−N−C (1:1) and (1:0.3) exhibited the highest MAs of 8.2 and 19.3 A g^{-1}, respectively. These values are significantly higher than that of the commercial Fe−N−C_{PMF} (4.8 A g^{-1}) and other state-of-the-art M−N−Cs reported in the literature (see also Supporting Information Table S4).[31,34] The notably high MA of Fe−Sn−N−C (1:0.3) is unequaled for PGM-free catalysts. The MA of this catalyst surpasses the MA of the commercial Pt/C_{Tanaka} in 0.5 mol L^{-1} H_3PO_4 (17.8 A g^{-1}) at 0.8 V_{RHE} (MA of Pt/C at 0.9 V_{RHE} see Table S4 in Supporting Information). Sn−N−C exhibits the lowest MA (0.6 A g^{-1}), followed by Fe−N−C (1.8 A g^{-1}). This indicates that tin, when considered independently as the Sn−N_x site, is not notably active for catalyzing the oxygen reduction. However, it has a significant impact on the activity when it is combined with iron, as evidenced by the substantial increase in activity.

To exclude that different iron and total metal contents influence the activity trend, the MA was normalized to the metal content and to the iron content determined by ICP−MS (Supporting Information Figure S8 and Table S4). This normalization indicates a comparable trend of activity among the MOF-based catalysts examined in this study, with the Fe−Sn−N−C (1:0.3) catalyst demonstrating the highest MA normalized to Fe and metal content. Consequently, enhanced activity cannot be attributed merely to comparatively higher iron contents.

As observed in the cyclic voltammograms (Supporting Information Figure S7), the bimetallic Fe−Sn−N−C catalysts exhibit a higher double layer capacitance in comparison with the other catalysts examined. This may indicate increased porosity or enhanced wettability with the electrolyte, potentially enhancing the accessibility of active sites. An increased double-layer capacity does not invariably correspond with an increased number of electrochemically active sites or enhanced mass activity. This is evidenced by the significantly higher activity observed for the Fe−Sn−N−C (1:0.3) compared to the Fe−Sn−N−C (1:1), despite exhibiting equivalent capacitive currents. Large surface areas present in M−N−C materials predominantly stem from carbon moieties that contribute to the double-layer capacitance, independent of directly affecting ORR activity.[55]

Second, the selectivity toward the 4-electron ORR mechanism was investigated. Therefore, the hydrogen peroxide yield during the RRDE measurements was determined from the ring currents at 0.2 and 0.7 V_{RHE} (Figure 5a,b). Fe−Sn−N−C (1:1) and (1:0.3) exhibited the lowest hydrogen peroxide yields at 0.2 V_{RHE} with values of 5.8 $\%_{H2O2}$ and 5.9

https://doi.org/10.1021/acscatal.4c06338
ACS Catal. 2025, 15, 4477−4488

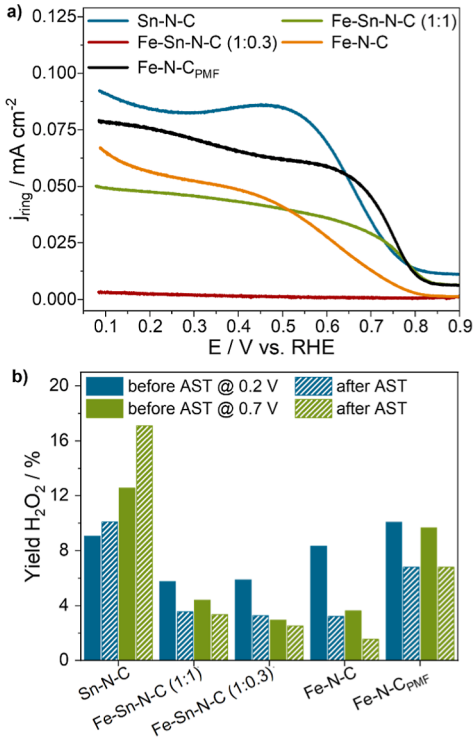

Figure 5. (a) Ring current densities during ORR measurements and (b) peroxide yields determined at 0.2 and 0.7 V_{RHE} from the ring current densities before and after the AST.

$\%_{H2O2}$, respectively. Fe−N−C and Sn−N−C reached higher peroxide yields with values of 8.3 $\%_{H2O2}$ and 9.1 $\%_{H2O2}$. The commercial Fe−N−C_{PMF} showed the highest peroxide yield of 10.1 $\%_{H2O2}$ (Figure 5b). At higher potentials (0.7 V_{RHE}), the H_2O_2 yields are decreased for the Fe−Sn−N−Cs with 4.4 $\%_{H2O2}$ and 2.9 $\%_{H2O2}$ for Fe−Sn−N−C (1:1) and Fe−Sn−N−C (1:0.3). This trend is in accordance with other Fe−Sn−N−C catalysts from the literature.[31] Also, lower peroxide yields at 0.7 V_{RHE} are measured for Fe−N−C with 3.6 $\%_{H2O2}$. The yield for Fe−N−C_{PMF} at 0.7 V_{RHE} is found to be at a comparable level of 9.7 $\%_{H2O2}$, falling within the range of deviation. In contrast, Sn−N−C exhibits an increase in yield at higher potentials to 12.6 $\%_{H2O2}$.

In summary, the Fe−Sn−N−Cs display much lower peroxide yields than the Fe−N−Cs and the Sn−N−C. This suggests efficient 4-electron pathways for ORR for these novel catalysts and minimal undesirable 2-electron pathways, which typically result in the formation of hydrogen peroxide.[59,60] A low H_2O_2 yield indicates the successful incorporation of the M−N_x centers and a low proportion of metal-free N functionalities. Similarly, high peroxide yields can have a disadvantageous effect on the stability of catalysts, as carbon decomposition and the associated degradation of active sites is triggered by H_2O_2.[17,50] There is no trend between the nitrogen content or nitrogen type and selectivity, although overall peroxide yields are low, so the trend could be suppressed, as even small measurement deviations can have an influence.

Next, an AST under harsh conditions was applied to assess the stability for all catalysts. The AST employs square wave cycling of the potential. This involves 10,000 sweeps between 0.6 and 1.0 V_{RHE} over 3 s intervals in an oxygen-saturated electrolyte. With this potential range, the formation of ROS should be provoked, which can cause the demetalation of metal−nitrogen sites and, to a lesser extent, corrosion of the carbon support structure.[61]

In addition to the high MA and good selectivity of the Fe−Sn−N−C (1:1), a remarkable stability is also demonstrated with an MA reduction of only −38 %, similar to the commercial Fe−N−C_{PMF} (−35 %) after AST, indicating a low degradation of the active sites (Figure 4b and Supporting Information Figure S7). This observation emphasizes the assumption that tin may exert a stability-enhancing effect on our Fe−N−Cs, in addition to an activity-enhancing effect. This effect could be achieved by an electronic effect of Sn on the Fe sites or by a direct influence of Sn on the reaction. However, the latter is less plausible given that monometallic Sn−N−C does not exhibit high activity and is unlikely to be directly involved in the reaction. However, the reduction of the tin content for the Fe−Sn−N−C (1:0.3), which resulted in an exceptionally high activity, also led to a lower stability, with a −71 % MA loss after AST. It is, albeit, noteworthy that even after subjecting the Fe−Sn−N−C (1:0.3) to a stress test, its MA exceeds the initial activity of the commercial Fe−N−C_{PMF} by 27 %. The lower MA loss of Fe−N−C (−37 %), compared to the high MA loss of Fe−Sn−N−C (1:0.3), can be associated with the lower initial activity, indicating that a smaller number of active sites could be degraded.

In addition to the measurement in phosphoric acid, RRDE tests were also carried out in commonly used diluted perchloric acid (Supporting Information Figure S8) to have an appropriate comparison with the recent literature. The MA in 0.1 mol L^{-1} $HClO_4$ of the Fe−Sn−N−C (1:1) with 5.1 A g^{-1} is still surpassing the activity of Fe−N−C_{PMF} with 1.8 A g^{-1} and also the activity of current state of the art M−N−Cs and recent Fe−Sn−N−C catalysts from other synthesis approaches (1.2 and 4.8 A g^{-1}), as shown in the Supporting Information Table S4.[31,34,42,46]

The stability of the Fe−N−C_{PMF} in $HClO_4$ is higher with a −7 % MA loss after the AST compared to the measurements in H_3PO_4. Thus, the Fe−N−C_{PMF} catalyst is more affected by phosphoric acid than Fe−Sn−N−C (1:1), which has similar mass loss independent of the electrolyte. It may be reasonably deduced that the preliminary activity of Fe−N−C_{PMF} is promoted by the phosphoric acid electrolyte, as previously discussed in the literature for Fe−N−Cs.[62] Holst-Olesen et al. propose the selective adsorption of phosphates to one site of the M−N_x centers, which may promote activity on the other side due to electronic effects.[62] A detailed discussion of current catalysts and the effect of the electrolytes is given in the Supporting Information. Table S4 shows that the prepared ZIF-based Fe−Sn−N−C catalysts exhibit remarkably high MA in the phosphoric acid electrolyte, even exceeding most platinum-containing catalysts in terms of total catalyst mass. Due to the low metal contents of Fe−Sn−N−C (1:1) and Fe−Sn−N−C (1:0.3) of 1.4 and 1.2 wt.%, respectively, the MA related to the metal content (at 0.8 V_{RHE} in 0.5 mol L^{-1} H_3PO_4: Fe−Sn−N−C (1:1) 0.57 A g^{-1}_{metal} and Fe−Sn−N−C (1:0.3) 1.60 A g^{-1}_{metal}) are also in the upper range of platinum-free catalysts (Supporting Information Figure S8 and Table S4). As an addition to the comprehensive RRDE study, a first HT-PEM single cell measurement with the most active Fe−Sn−N−C catalyst was performed (Supporting Information Figure S10). This test showed a peak power density of 53 mW cm^{-2}, which is lower compared to the MEA with commercial Fe−N−C_{PMF} (106 mW cm^{-2}), but within the range of other newly developed M−N−C catalysts (CoFe−N−SiOCa:[26] 50

https://doi.org/10.1021/acscatal.4c06338
ACS Catal. 2025, 15, 4477−4488

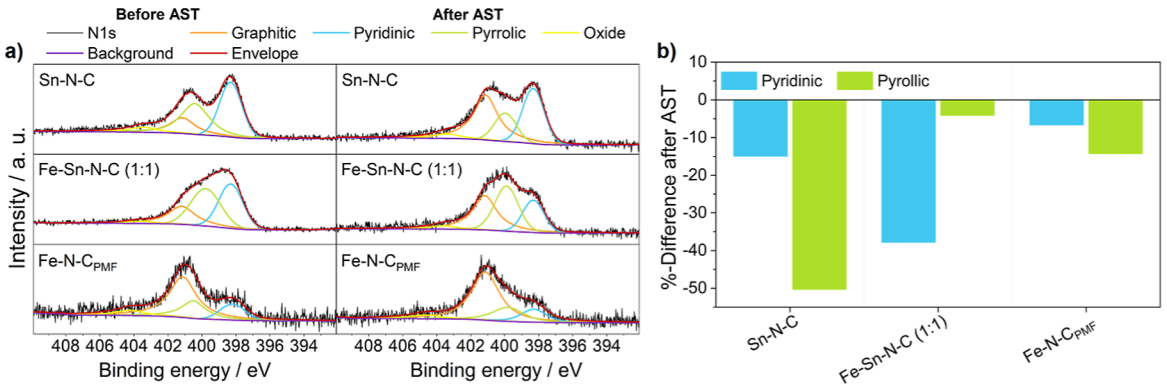

Figure 6. (a) N 1s high-resolution XP spectra of the catalyst layers with peak fitting and (b) determined loss of proportions of *N*-species (pyridinic and pyrrolic) before and after the AST.

mW cm^{-2} and Fe−N-ox-BP:[63] 67 mW cm^{-2}). As shown in Supporting Information (Figure S10), It is evident that there is a necessity for electrode fabrication, including ink composition, e.g., binder content and solvent, as well as the coating procedure, to maximize the activity of the catalyst in HT-PEMFC.[63−65]

2.3. Physical Analyses before and after AST. For a more detailed analysis of catalyst degradation, Sn−N−C, Fe−Sn−N−C (1:1), and Fe−N−C$_{PMF}$ were selected for additional grazing incident XRD (GIXRD) and XPS measurements (Supporting Information Figure S9). The catalyst layers were characterized directly on the glassy carbon (GC) disc of RRDE before and after AST. The GIXRD results (Supporting Information Figure S9a) showed no significant changes in the crystal structure of the catalysts after AST. This suggests that this AST does not cause severe formation of ORR-inactive metallic particles, which is essential to maintain active catalytic sites.

The XPS analysis (Figure 6 and Supporting Information Figure S9b−d) focused on changes in the oxidation states and bonding environments of nitrogen because of interfering signals from the ionomer (Nafion^{TM}) with respect to carbon, oxygen, and an energy loss signal from fluorine, which affected the iron spectra. Detailed peak fitting, analogous to the catalyst powder fittings, showed changes in the types of nitrogen bonds present in the catalysts (Figures 6 and S9c). A decrease in pyridinic and pyrrolic nitrogen species with overall losses from −32 % for the Sn−N−C, −21 % for Fe−Sn−N−C (1:1), and −11 % for Fe−N−C$_{PMF}$ are detected. This reduction is significant, as these nitrogen configurations are crucial for catalytic activity when forming an M−N$_x$ site, therefore indicating a loss of active centers. Interestingly, the Fe−N−C$_{PMF}$ catalyst showed only small changes in nitrogen species, indicating a different degradation behavior compared to that of MOF-based catalysts (Figures 6 and S9c). The loss of pyridinic nitrogen is higher in the Fe−Sn−N−C with −38 % than in the Sn−N−C with −15 % (Figure 6b in blue). On the other hand, the degradation of pyrrolic nitrogen is higher in the Sn−N−C with a decrease of 50 % than in the Fe−Sn−N−C with a reduction of only 4 % (Figure 6b in green). The differences in N species loss of pyridinic and pyrrolic nitrogen suggest that the incorporation in the catalytic structure is different in the two catalysts. Furthermore, an examination of the Sn 3d high-resolution XP spectra (Supporting Information Figure 9d) revealed no significant differences, suggesting that the character of the tin species remains unchanged, and there is no substantial loss of tin.

While the analyzed physical structure of the catalysts remained intact, as evidenced by the GIXRD results, the chemical changes observed by XPS indicate that the active sites are vulnerable to operational conditions. It can be concluded that the loss of activity due to the AST is likely attributed to the loss of active sites. However, the absence of metallic particles and the lack of significant loss of tin observed in the XPS data suggest that these active sites may not have been M−N$_x$ sites. This assumption is further fortified by the enhanced selectivity of the Fe−Sn−N−C catalysts after the AST, thereby indicating that a higher proportion of metal-free pyridinic and pyrrolic sites are lost.

3. CONCLUSIONS

The activity, stability, and selectivity of ZIF-based Fe−Sn−N−Cs toward the ORR in acidic medium in comparison to monometallic Sn−N−C and Fe−N−Cs were investigated in this study. ZIF-8-based catalysts were prepared in different metal ratios, obtaining the catalysts Sn−N−C, Fe−N−C, Fe−Sn−N−C (1:1), and Fe−Sn−N−C (1:0.3). Via physical characterization in comparison to the commercial Fe−N−C$_{PMF}$, the success of the synthesis was confirmed. The nitrogen content in the synthesized catalysts (14−20 at.%), which predominantly contain ORR-active nitrogen species (pyridinic, pyrrolic, and graphitic), is significantly higher than that of the commercial Fe−N−C$_{PMF}$ (7 at.%).

The catalysts exhibit high reproducibility with respect to the electrochemical measurements in 0.5 mol L^{-1} H_3PO_4 and differ in terms of the ORR performance, with the MA (at 0.8 V_{RHE}) of Fe−Sn−N−C (1:1) reaching 8.2 A g^{-1}, clearly exceeding Fe−N−C$_{PMF}$ with 4.8 A g^{-1}. In contrast, the Sn−N−C and Fe−N−C have relatively low MA at 0.6 and 1.8 A g^{-1}, respectively. By reducing the tin content, Fe−Sn−N−C (1:0.3) was obtained and yielded an extraordinarily high MA of 19.3 A g^{-1} at 0.8 V_{RHE}. Similarly, Fe−Sn−N−C (1:1) exhibits an MA of 5.1 A g^{-1} in commonly used 0.1 mol L^{-1} $HClO_4$, which is unparalleled by current state-of-the-art M−N−Cs.

The application of a harsh AST resulted in the determination of good stability in H_3PO_4 (MA loss of −38 %) for Fe−Sn−N−C (1:1), which was comparable to that of Fe−N−C$_{PMF}$. The reduction in tin content led to a loss of stability in the Fe−Sn−N−C (1:0.3), resulting in an MA loss of −71 % after the AST. However, the still very high activity of 5.6 A g^{-1} after the AST is remarkable. Although the DAC

https://doi.org/10.1021/acscatal.4c06338
ACS Catal. 2025, 15, 4477−4488

character of the catalysts could not be confirmed, the beneficial effect of the Sn is undoubtedly present, as evidenced by the markedly high activities observed even with relatively low amounts of tin. It was proposed that tin may act as a structural promoter for iron, thereby improving the performance. The hypothesis is based on two potential assumptions. The first posits direct involvement of tin in the redox reaction. The second, and potentially more plausible, assumption assumes an electronic effect of the tin on the Fe sites, despite the presumed lack of a direct neighborhood between the two elements. These interactions have the potential to influence chemical reaction pathways, thereby opening avenues for enhancing the material efficiency. Additionally, it has been demonstrated that the metal ratio of 1:1, which has been a popular choice in the literature, may not necessarily represent the optimal catalyst, as even low levels of Sn have been shown to significantly enhance the activity.

Degradation analyses by GIXRD and XPS demonstrated a reduction in pyridinic and pyrrolic bound nitrogen in the catalysts, indicating the depletion of active sites. Given that no distinct formation of metallic particles or loss of metal was observed, it can be assumed that there has been a loss of nonmetallic nitrogen sites. This is evidenced by the high activity of Fe−Sn−N−C (1:1) after AST.

In response to the promising activity and selectivity of these Fe−Sn−N−C catalysts, further systematic investigations of the Fe/Sn ratio are planned. Also, further physical (i.e., XAS and ^{119}Sn−Mössbauer) and electrochemical analysis of the catalysts, to gain a deeper understanding of their structural characteristics, the nature of the metal sites present, and the correlation between iron and tin, is pursued. Moreover, subsequent steps will entail efforts to optimize the electrodes for HT-PEMFC testing.

4. MATERIALS AND METHODS

4.1. Catalyst Preparation. For ZIF-8 synthesis, zinc(II)-nitrate hexahydrate (2.232 g, 7.50 mmol, 1 equiv, Carl Roth, ≥99 %) was added to 100 mL of methanol (Carl Roth, ≥99 %, p.a.) in a round-bottom flask and stirred for 15 min. Then, 2-methylimidazole (2.464 g, 30.01 mmol, 4 eq, Sigma-Aldrich, p.a.) was weighed in a glovebox under a N_2 atmosphere and dissolved in 100 mL methanol under an air atmosphere. The solution was added to the zinc(II)nitrate solution with stirring, and a white precipitate formed after a few minutes. The mixture was stirred for at least 6 h at room temperature in a sealed round-bottom flask, followed by centrifugation to obtain the white precipitate, three washing steps with 30 mL of methanol, and drying in a vacuum.

For tin doping, a tin solution in methanol was prepared (tin acetate, 50 mg mL^{-1}, Sigma-Aldrich, p.a.) and, according to Table S1, dropped to the ZIF-8 (500 mg in 10 mL methanol) in an ultrasonic bath at room temperature, followed by 2 h of sonication. The Sn-doped ZIF-8 was centrifuged and dried in a vacuum oven at 40 °C.

For the preparation of the Fe−Sn−N−Cs, a second doping with an iron solution (iron chloride, 50 mg mL^{-1}, Sigma-Aldrich, p.a.) was carried out. 500 mg of Sn-doped ZIF-8 were dispersed in 10 mL of methanol, treated for 30 min in an ultrasonic bath, and doped with 250 μL of the Fe solution. After ultrasonic treatment for 2 h, centrifugation, and drying in a vacuum oven, a light-yellow powder was obtained.

Subsequently, the doped ZIF-8 was weighed into ceramic boats and treated in a tube furnace with a ceramic tube (RHTC 80-230/15, Nabertherm) with a heating rate of 5 K min^{-1} to 1000 °C under a nitrogen flow (100 L h^{-1}). The temperature was maintained for 2 h before cooling to room temperature at 5 K min^{-1}.

4.2. Physical Characterization. *4.2.1. Elemental Analysis by ICP−MS.* ICP−MS was used to quantitatively analyze the iron and tin content of the samples (Table S1). Catalyst (5 mg) was weighed into a Teflon insert, and 3.45 mL of concentrated HCl (Carl Roth, Supra, 35 %) and 1.56 mL of concentrated HNO_3 (Carl Roth, Supra, 69 %) were added. The insert was then sealed with a lid and placed in a 250 mL stainless steel autoclave. The autoclave was closed with a torque wrench (25 Nm) and stored for 18 h at 220 °C in an oven, followed by cooling to room temperature. The obtained solution was diluted to 150 mL with HNO_3 (2 vol.%) and then measured via ICP−MS. Samples were analyzed using an iCapQ instrument (Thermo Fisher). An internal scandium standard (1000 mg L^{-1}, Carl Roth) and corresponding iron or tin (Carl Roth) were used for calibration, with concentrations of 0.5, 5, 50, 100, 200, 300, and 500 μg L^{-1}. A correlation coefficient of at least 0.999 was ensured for calibration.

4.2.2. TEM. For TEM measurements, 1 mg of catalyst was dispersed in 1 mL of ethanol (Carl Roth, p.a.) and treated in an ultrasonic bath for 10 min. Five μL of the dispersion was dropped onto a copper mesh with polyvinyl formal film (200 mesh, Plano) and dried for 5 min. ZEISS EM 900N TEM with a tungsten cathode and an accelerating voltage of 80 kV was used. For HR-TEM and STEM/EDS analysis, a Jeol JEM2100 F with an acceleration voltage of 200 kV was used. For the STEM/EDS Oxford INCA Energy TEM250 EDS system with an XMAX80 silicon drift detector was used, and EDS mapping was performed with a magnification of 200,000, recording approximately 1,000,000 pulses.

4.2.3. PXRD. Powder diffractograms were measured on an Empyrean Series 2 diffractometer (PANanalytical) in Bragg−Brentano geometry and under Cu Kα radiation. The catalysts (10 mg) were dispersed in 0.5 mL of 2-propanol (Carl Roth) in an ultrasonic bath for 15 min and then dropped onto a zero-background silica holder. A scan range between 5° and 70° was measured at a voltage of 40 kV and a current of 40 mA. For data evaluation, HighScore Plus software (PANanalytical) was used.

4.2.4. XPS. For XPS analyses, an ESCALAB 250Xi (Thermo Fisher) was used with monochromatic Al- Kα radiation and a beam diameter of 650 μm. Three survey scans were recorded, using a transit energy of 100 eV, a dwell time of 20 ms, and a step size of 1 eV. Furthermore, high-resolution spectra for the elements C (1s, 3 scans), O (1s, 5 scans), N (1s, 10 scans), Fe (2p, 10 scans), Sn (3d, 10 scans), and Zn (2p, 3 scans) were recorded. A transit energy of 20 eV, a dwell time of 50 ms, and a step size of 0.02 eV were used. The Avantage software (Thermo Fisher) was used with a smart background and Gauss-Lorentz line shape for peak fitting.

4.2.5. ^{57}Fe Mössbauer. The Mössbauer measurements were conducted in transmission geometry with a custom-made miniaturized Mössbauer spectrometer (MIMOS II). A Co-57/Rh source was utilized, with measurements recorded at 14.4 keV. Data analysis was conducted using Recoil software (Rancourt and Ping, 2003). The velocity scale and isomer shift were calibrated with α-Fe (iron foil with 2.14 % Fe-57, 20 μm, 99.85 % purity).

4.3. Electrochemical Analysis. The electrochemical characterization was carried out using an RRDE with a GC

https://doi.org/10.1021/acscatal.4c06338
ACS Catal. 2025, 15, 4477−4488

disk (0.2472 cm^2) and a platinum ring (0.1859 cm^2) with a collector efficiency of 37 % (AFE7R9GCPT, Pine Research Instrumentation). First, the RRDE was polished with 1.00 and 0.05 μm aluminum oxide abrasive suspension (MicroPolish, BUEHLER) for 5 min each, and subsequently ultrasonicated in 2-propanol, followed by water for 5 min. For the catalyst ink, 6 mg of the catalyst, 561.6 μL of ultrapure water, and 126 μL of 2-propanol were mixed and treated for 15 min in an ultrasonic bath. Subsequently, 76.2 μL of a Nafion solution (5 wt.% in aliphatic alcohols, Sigma-Aldrich) was added, and the ink was further mixed in a sonication bath for 5 min and for 4 min treated via horn sonification (amplitude 10 %, 30 s on, 30 s off). Then, 12.6 μL of the ink were dropped onto the GC disc and dried for 5 min at 60 °C to obtain a final catalyst loading of 400 $\mu g\ cm^{-2}$. In order to compare the MA, also a Tanaka Pt/C catalyst (TEC10E40E, 40 wt.% Pt on high surface area carbon) was assessed.

A GC rod (Redox.me) was used as the counter electrode and a reversible hydrogen electrode (HydroFlex, Gaskatel) as the reference electrode. The electrodes were separated from the working electrode by glass frites. Measurements were carried out in 0.5 mol L^{-1} H_3PO_4 (Carl Roth, p.a.) or 0.1 mol L^{-1} $HClO_4$ (Merck, p.a.) as electrolyte in a glass cell. PGSTAT204 potentiostat (Metrohm Autolab) and NOVA 2.1 software were used. For the initial characterization, the electrolyte was saturated with O_2 for 15 min, followed by three CVs at a rotation of 1600 rpm between 0.05 and 1.05 V_{RHE} with 5 mV s^{-1} and a constant ring potential of 1.2 V_{RHE}. The second and third anodic scans were averaged for the evaluation. Three CVs without rotation were subsequently recorded with the same parameters in a N_2-saturated electrolyte for background correction. Next, impedance spectroscopy at 0.3 V with an amplitude of 10 mV and a frequency range of 100 kHz to 0.1 Hz for the correction of the potentials by the electrolyte resistance. To complete the initial characterization, five CVs in the potential range of 0.05−1.00 V_{RHE} at 50 mV s^{-1} were recorded. To provoke degradation of the metal sites, the electrolyte was saturated with O_2 for the AST, and the potential was cycled 10,000 times between 0.6 and 1.0 V_{RHE}.[66] The subsequent final characterization was performed in a manner analogous to the initial characterization. For each catalyst, three independent measurements were made and averaged.

The MA was calculated from the ORR polarization curves using the current density at 0.8 V_{RHE}, the average of the diffusion-limited current density j_{lim} in the diffusion-limited area (0.1 and 0.4 V_{RHE}), and the catalyst loading ($m_{catalyst}$) of 400 $\mu g\ cm^{-2}$ in eq 1.

$$\mathrm{MA} = \frac{j_{0.8\mathrm{V}} \times j_{\mathrm{lim}}}{j_{\mathrm{lim}} - j_{0.8\mathrm{V}}} \times \mathrm{m}_{\mathrm{catalyst}}^{-1} \tag{1}$$

The H_2O_2 yield was calculated according to eq 2, with a ring collection efficiency N = 37 % given by the manufacturer and the background corrected disc potential (j_{disc}).

$$H_2O_2\ \text{yield} = \frac{\frac{2 \times j_{\mathrm{ring}}}{N}}{j_{\mathrm{disc}} + \frac{j_{\mathrm{ring}}}{N}} \times 100 \tag{2}$$

4.4. Degradation Analysis. In order to investigate the degradation caused by the AST, physical analyses were carried out before and after. To measure the catalyst layer, exchangeable RRDEs were used (AFE6R1PT, Pine Research Instrumentation) with a GC disk (0.1963 cm^2) and a platinum ring (0.1100 cm^2) with a collector efficiency of 26 %. The electrode and catalyst ink were prepared, as described for the electrochemical measurement, and coated with 2 × 12.6 μL for clearer results (total loading of 0.8 mg cm^{-2}). The coated disc was analyzed by XPS and GIXRD before and after AST in 0.5 mol L^{-1} H_3PO_4 (Carl Roth, p.a.).

■ ASSOCIATED CONTENT

Supporting Information

The Supporting Information is available free of charge at https://pubs.acs.org/doi/10.1021/acscatal.4c06338.

Catalyst synthesis scheme, pyrolysis temperature experiments, catalyst metal ratios (applied and ICP−MS), TEM picture of ZIF-8, PXRD measurements, fitted XPS spectra, Mössbauer spectra and parameters, RRDE in H_3PO_4 electrolyte (polarization curves, CVs, Tafel plots, H_2O_2 yield), RRDE polarization curves in $HClO_4$ electrolyte, results of degradation analyses (GIXRD, XPS), HT-PEMFC measurements and discussion and literature comparison of MAs for ORR catalysts in acidic electrolytes (PDF)

■ AUTHOR INFORMATION

Corresponding Author

Julia G. Buschermöhle − *Institute of Engineering Thermodynamics, German Aerospace Center (DLR), Oldenburg 26129, Germany; Institute of Chemistry, Carl von Ossietzky University Oldenburg, Oldenburg 26129, Germany;* orcid.org/0000-0002-0414-9756; Email: julia.buschermoehle@dlr.de

Authors

Julia Müller-Hülstede − *Institute of Engineering Thermodynamics, German Aerospace Center (DLR), Oldenburg 26129, Germany;* orcid.org/0000-0001-7822-8425

Henrike Schmies − *Institute of Engineering Thermodynamics, German Aerospace Center (DLR), Oldenburg 26129, Germany*

Dana Schonvogel − *Institute of Engineering Thermodynamics, German Aerospace Center (DLR), Oldenburg 26129, Germany;* orcid.org/0000-0002-2485-740X

Tanja Zierdt − *Institute of Engineering Thermodynamics, German Aerospace Center (DLR), Oldenburg 26129, Germany*

Rene Lucka − *Institute of Inorganic Chemistry, Leibniz University Hannover, Hannover 30167, Germany*

Franz Renz − *Institute of Inorganic Chemistry, Leibniz University Hannover, Hannover 30167, Germany;* orcid.org/0000-0003-1494-1242

Peter Wagner − *Institute of Engineering Thermodynamics, German Aerospace Center (DLR), Oldenburg 26129, Germany;* orcid.org/0000-0002-5644-9881

Michael Wark − *Institute of Chemistry, Carl von Ossietzky University Oldenburg, Oldenburg 26129, Germany;* orcid.org/0000-0002-8725-0103

Complete contact information is available at: https://pubs.acs.org/10.1021/acscatal.4c06338

Notes

The authors declare no competing financial interest.

https://doi.org/10.1021/acscatal.4c06338
ACS Catal. 2025, 15, 4477−4488

■ ACKNOWLEDGMENTS

This research was carried out in frame of the project HT-PEM 2.0 funded by Federal Ministry for Economic Affairs and Climate Action on the basis of a decision by the German Bundestag, grant number 03ETB016A. We thank Jana Ewert for ICP−MS measurements, as well as Jasmin Schmeling for valuable assistance with TEM measurements and Stefanie Laue for assistance with part of the HT-PEMFC measurements (all DLR). The authors acknowledge the Electron and Light Microscopy Service Unit, Carl von Ossietzky University of Oldenburg, for the use of the imaging facilities, as well as the Leibniz University Hannover for the use of the Mössbauer facilities with funding from the MIMOS projects (FKZ 50OO2415, 50OO2214, and 50OO2104). The XPS and XRD instruments are funded by DFG through grants INST 184/144-1 FUGG and INST 184/154-1 FUGG.

■ REFERENCES

(1) Staffell, I.; Scamman, D.; Velazquez Abad, A.; Balcombe, P.; Dodds, P. E.; Ekins, P.; Shah, N.; Ward, K. R. The role of hydrogen and fuel cells in the global energy system. *Energy Environ. Sci.* **2019**, *12* (2), 463−491.

(2) Haider, R.; Wen, Y.; Ma, Z.-F.; Wilkinson, D. P.; Zhang, L.; Yuan, X.; Song, S.; Zhang, J. High temperature proton exchange membrane fuel cells: progress in advanced materials and key technologies. *Chem. Soc. Rev.* **2021**, *50* (2), 1138−1187.

(3) Maiyalagan, T.; Pasupathi, S. Components for PEM Fuel Cells: An Overview. *Mater. Sci. Forum* **2010**, *657*, 143−189.

(4) Li, Q.; He, R.; Gao, J.-A.; Jensen, J. O.; Bjerrum, N. J. The CO Poisoning Effect in PEMFCs Operational at Temperatures up to 200°C. *J. Electrochem. Soc.* **2003**, *150* (12), A1599−A1605.

(5) Zhai, Y.; Bender, G.; Dorn, S.; Rocheleau, R. The Multiprocess Degradation of PEMFC Performance Due to Sulfur Dioxide Contamination and Its Recovery. *J. Electrochem. Soc.* **2010**, *157* (1), B20.

(6) Chandan, A.; Hattenberger, M.; El-Kharouf, A.; Du, S.; Dhir, A.; Self, V.; Pollet, B. G.; Ingram, A.; Bujalski, W. High temperature (HT) polymer electrolyte membrane fuel cells (PEMFC) − A review. *J. Power Sources* **2013**, *231* (0), 264−278.

(7) Rosli, R. E.; Sulong, A. B.; Daud, W.; Zulkifley, M. A.; Husaini, T.; Rosli, M. I.; Majlan, E. H.; Haque, M. A. A review of high-temperature proton exchange membrane fuel cell (HT-PEMFC) system. *Int. J. Hydrogen Energy* **2017**, *42* (14), 9293−9314.

(8) Renau, J.; Barroso, J.; Lozano, A.; Nueno, A.; Sánchez, F.; Martín, J.; Barreras, F. Design and manufacture of a high-temperature PEMFC and its cooling system to power a lightweight UAV for a high altitude mission. *Int. J. Hydrogen Energy* **2016**, *41* (43), 19702−19712.

(9) Friedrich, K. A.; Kallo, J.; Schirmer, J.; Schmitthals, G. Fuel Cell Systems for Aircraft Application. *ECS Trans.* **2009**, *25* (1), 193−202.

(10) Li, Q. High Temperature Polymer Electrolyte Membrane Fuel Cells. In *Approaches, Status, and Perspectives*; Springer International Publishing, 2015.

(11) Xue, D.; Zhang, J.-N. Recent progress of antipoisoning catalytic materials for high temperature proton exchange membrane fuel cells doped with phosphoric acid. *Ind. Chem. Mater.* **2024**, *2* (2), 173−190.

(12) Meyer, Q.; Yang, C.; Cheng, Y.; Zhao, C. Overcoming the Electrode Challenges of High-Temperature Proton Exchange Membrane Fuel Cells. *Electrochem. Energy Rev.* **2023**, *6* (1), 16.

(13) Zeis, R. Materials and characterization techniques for high-temperature polymer electrolyte membrane fuel cells. *Beilstein J. Nanotechnol.* **2015**, *6*, 68−83.

(14) Bevilacqua, N.; Asset, T.; Schmid, M. A.; Markötter, H.; Manke, I.; Atanassov, P.; Zeis, R. Impact of catalyst layer morphology on the operation of high temperature PEM fuel cells. *J. Power Sources Adv.* **2021**, *7*, 100042.

(15) Wang, Y.; Ruiz Diaz, D. F.; Chen, K. S.; Wang, Z.; Adroher, X. C. Materials, technological status, and fundamentals of PEM fuel cells − A review. *Mater. Today* **2020**, *32*, 178−203.

(16) Artyushkova, K.; Serov, A.; Rojas-Carbonell, S.; Atanassov, P. Chemistry of Multitudinous Active Sites for Oxygen Reduction Reaction in Transition Metal−Nitrogen−Carbon Electrocatalysts. *J. Phys. Chem. C* **2015**, *119* (46), 25917−25928.

(17) Martinaiou, I.; Shahraei, A.; Grimm, F.; Zhang, H.; Wittich, C.; Klemenz, S.; Dolique, S. J.; Kleebe, H.-J.; Stark, R. W.; Kramm, U. I. Effect of metal species on the stability of Me-N-C catalysts during accelerated stress tests mimicking the start-up and shut-down conditions. *Electrochim. Acta* **2017**, *243*, 183−196.

(18) Proietti, E.; Jaouen, F.; Lefèvre, M.; Larouche, N.; Tian, J.; Herranz, J.; Dodelet, J.-P. Iron-based cathode catalyst with enhanced power density in polymer electrolyte membrane fuel cells. *Nat. Commun.* **2011**, *2*, 416.

(19) Gasteiger, H. A.; Kocha, S. S.; Sompalli, B.; Wagner, F. T. Activity benchmarks and requirements for Pt, Pt-alloy, and non-Pt oxygen reduction catalysts for PEMFCs. *Appl. Catal., B* **2005**, *56* (1−2), 9−35.

(20) Cui, J.; Chen, Q.; Li, X.; Zhang, S. Recent advances in non-precious metal electrocatalysts for oxygen reduction in acidic media and PEMFCs: an activity, stability and mechanism study. *Green Chem.* **2021**, *23* (18), 6898−6925.

(21) Shao, Y.; Dodelet, J.-P.; Wu, G.; Zelenay, P. PGM-Free Cathode Catalysts for PEM Fuel Cells: A Mini-Review on Stability Challenges. *Adv. Mater.* **2019**, *31* (31), 1807615.

(22) Müller-Hülstede, J.; Schmies, H.; Schonvogel, D.; Meyer, Q.; Nie, Y.; Zhao, C.; Wagner, P.; Wark, M. What determines the stability of Fe-N-C catalysts in HT-PEMFCs? *Int. J. Hydrogen Energy* **2024**, *50*, 921−930.

(23) Zierdt, T.; Reuter, T.; Müller-Hülstede, J.; Buschermöhle, J.; Schonvogel, D.; Kröner, J.; Schwan, M.; Milow, B.; Wagner, P.; Andreas Friedrich, K. Impact of Aerogel Modification for Fe-N-C Activity and Stability towards Oxygen Reduction Reaction in Phosphoric Acid Electrolyte. *ChemSusChem* **2024**, No. e202401843.

(24) Wang, J.; Huang, Z.; Liu, W.; Chang, C.; Tang, H.; Li, Z.; Chen, W.; Jia, C.; Yao, T.; Wei, S.; Wu, Y.; Li, Y. Design of N-Coordinated Dual-Metal Sites: A Stable and Active Pt-Free Catalyst for Acidic Oxygen Reduction Reaction. *J. Am. Chem. Soc.* **2017**, *139* (48), 17281−17284.

(25) Mehmood, A.; Gong, M.; Jaouen, F.; Roy, A.; Zitolo, A.; Khan, A.; Sougrati, M.-T.; Primbs, M.; Bonastre, A. M.; Fongalland, D.; Drazic, G.; Strasser, P.; Kucernak, A. High loading of single atomic iron sites in Fe−NC oxygen reduction catalysts for proton exchange membrane fuel cells. *Nat. Catal.* **2022**, *5* (4), 311−323.

(26) Mooste, M.; Müller-Hülstede, J.; Schonvogel, D.; Zierdt, T.; Buschermöhle, J.; Fuhrmann, K.; Wilhelm, M.; Wagner, P.; Friedrich, K. A. Binary transition metal and ZIF-8 functionalised polymer-derived ceramic catalysts for high temperature PEM fuel cell cathode. *Electrochim. Acta* **2025**, *514*, 145620.

(27) He, Y.; Tan, Q.; Lu, L.; Sokolowski, J.; Wu, G. Metal-Nitrogen-Carbon Catalysts for Oxygen Reduction in PEM Fuel Cells: Self-Template Synthesis Approach to Enhancing Catalytic Activity and Stability. *Electrochem. Energy Rev.* **2019**, *2* (2), 231−251.

(28) Pedersen, A.; Barrio, J.; Li, A.; Jervis, R.; Brett, D. J. L.; Titirici, M. M.; Stephens, I. E. L. Dual-Metal Atom Electrocatalysts: Theory, Synthesis, Characterization, and Applications. *Adv. Energy Mater.* **2022**, *12* (3), 2102715.

(29) Müller-Hülstede, J.; Uhlig, L. M.; Schmies, H.; Schonvogel, D.; Meyer, Q.; Nie, Y.; Zhao, C.; Vidakovic, J.; Wagner, P. Towards the Reduction of Pt Loading in High Temperature Proton Exchange Membrane Fuel Cells - Effect of Fe-N-C in Pt-Alloy Cathodes. *ChemSusChem* **2023**, *16* (5), No. e202202046.

(30) Liu, H.; Rong, H.; Zhang, J. Synergetic Dual-Atom Catalysts: The Next Boom of Atomic Catalysts. *ChemSusChem* **2022**, *15* (16), No. e202200498.

(31) Luo, F.; Roy, A.; Sougrati, M. T.; Khan, A.; Cullen, D. A.; Wang, X.; Primbs, M.; Zitolo, A.; Jaouen, F.; Strasser, P. Structural

https://doi.org/10.1021/acscatal.4c06338
ACS Catal. 2025, 15, 4477−4488

and Reactivity Effects of Secondary Metal Doping into Iron-Nitrogen-Carbon Catalysts for Oxygen Electroreduction. *J. Am. Chem. Soc.* **2023**, *145* (27), 14737−14747.
(32) Li, R.; Wang, D. Superiority of Dual-Atom Catalysts in Electrocatalysis: One Step Further Than Single-Atom Catalysts. *Adv. Energy Mater.* **2022**, *12* (9), 2103564.
(33) Gollasch, M.; Müller-Hülstede, J.; Schmies, H.; Schonvogel, D.; Wagner, P.; Dyck, A.; Wark, M. Elucidating Synergistic Effects of Different Metal Ratios in Bimetallic Fe/Co-N-C Catalysts for Oxygen Reduction Reaction. *Catalysts* **2021**, *11* (7), 841.
(34) Mazzucato, M.; Gavioli, L.; Balzano, V.; Berretti, E.; Rizzi, G. A.; Badocco, D.; Pastore, P.; Zitolo, A.; Durante, C. Synergistic Effect of Sn and Fe in Fe-Nx Site Formation and Activity in Fe-N-C Catalyst for ORR. *ACS Appl. Mater. Interfaces* **2022**, *14* (49), 54635−54648.
(35) Ye, W.; Chen, S.; Lin, Y.; Yang, L.; Chen, S.; Zheng, X.; Qi, Z.; Wang, C.; Long, R.; Chen, M.; Zhu, J.; Gao, P.; Song, L.; Jiang, J.; Xiong, Y. Precisely Tuning the Number of Fe Atoms in Clusters on N-Doped Carbon toward Acidic Oxygen Reduction Reaction. *Chem* **2019**, *5* (11), 2865−2878.
(36) Chu, Y.; Luo, E.; Wei, Y.; Zhu, S.; Wang, X.; Yang, L.; Gao, N.; Wang, Y.; Jiang, Z.; Liu, C.; Ge, J.; Xing, W. Dual single-atom catalyst design to build robust oxygen reduction electrode via free radical scavenging. *Chem Catal.* **2023**, *3* (3), 100532.
(37) Wang, F.; Xie, W.; Yang, L.; Xie, D.; Lin, S. Revealing the importance of kinetics in N-coordinated dual-metal sites catalyzed oxygen reduction reaction. *J. Catal.* **2021**, *396*, 215−223.
(38) Zhang, Y.; Evans, J. R. G.; Yang, S. Corrected Values for Boiling Points and Enthalpies of Vaporization of Elements in Handbooks. *J. Chem. Eng. Data* **2011**, *56* (2), 328−337.
(39) Liu, S.; Meyer, Q.; Li, Y.; Zhao, T.; Su, Z.; Ching, K.; Zhao, C. Fe−N−C/Fe nanoparticle composite catalysts for the oxygen reduction reaction in proton exchange membrane fuel cells. *Chem. Commun.* **2022**, *58* (14), 2323−2326.
(40) Serov, A.; Workman, M. J.; Artyushkova, K.; Atanassov, P.; McCool, G.; McKinney, S.; Romero, H.; Halevi, B.; Stephenson, T. Highly stable precious metal-free cathode catalyst for fuel cell application. *J. Power Sources* **2016**, *327*, 557−564.
(41) Alam, M.; Ping, K.; Danilson, M.; Mikli, V.; Käärik, M.; Leis, J.; Aruväli, J.; Paiste, P.; Rähn, M.; Sammelselg, V.; Tammeveski, K.; Haller, S.; Kramm, U. I.; Starkov, P.; Kongi, N. Iron Triad-Based Bimetallic M-N-C Nanomaterials as Highly Active Bifunctional Oxygen Electrocatalysts. *ACS Appl. Energy Mater.* **2024**, *7* (9), 4076−4087.
(42) Luo, F.; Roy, A.; Silvioli, L.; Cullen, D. A.; Zitolo, A.; Sougrati, M. T.; Oguz, I. C.; Mineva, T.; Teschner, D.; Wagner, S.; Wen, J.; Dionigi, F.; Kramm, U. I.; Rossmeisl, J.; Jaouen, F.; Strasser, P. P-block single-metal-site tin/nitrogen-doped carbon fuel cell cathode catalyst for oxygen reduction reaction. *Nat. Mater.* **2020**, *19* (11), 1215−1223.
(43) Asset, T.; Atanassov, P. Iron-Nitrogen-Carbon Catalysts for Proton Exchange Membrane Fuel Cells. *Joule* **2020**, *4* (1), 33−44.
(44) Martinez, U.; Komini Babu, S.; Holby, E. F.; Chung, H. T.; Yin, X.; Zelenay, P. Progress in the Development of Fe-Based PGM-Free Electrocatalysts for the Oxygen Reduction Reaction. *Adv. Mater.* **2019**, *31* (31), 1806545.
(45) Peng, H.; Liu, F.; Liu, X.; Liao, S.; You, C.; Tian, X.; Nan, H.; Luo, F.; Song, H.; Fu, Z.; Huang, P. Effect of Transition Metals on the Structure and Performance of the Doped Carbon Catalysts Derived From Polyaniline and Melamine for ORR Application. *ACS Catal.* **2014**, *4* (10), 3797−3805.
(46) Hu, Y.; Jensen, J. O.; Pan, C.; Cleemann, L. N.; Shypunov, I.; Li, Q. Immunity of the Fe-N-C catalysts to electrolyte adsorption: Phosphate but not perchloric anions. *Appl. Catal., B* **2018**, *234*, 357−364.
(47) Artyushkova, K.; Levendosky, S.; Atanassov, P.; Fulghum, J. XPS Structural Studies of Nano-composite Non-platinum Electrocatalysts for Polymer Electrolyte Fuel Cells. *Top. Catal.* **2007**, *46* (3), 263−275.
(48) Li, J.; Sougrati, M. T.; Zitolo, A.; Ablett, J. M.; Oğuz, I. C.; Mineva, T.; Matanovic, I.; Atanassov, P.; Huang, Y.; Zenyuk, I.; Di Cicco, A.; Kumar, K.; Dubau, L.; Maillard, F.; Dražić, G.; Jaouen, F. Identification of durable and non-durable FeNx sites in Fe−N−C materials for proton exchange membrane fuel cells. *Nat. Catal.* **2021**, *4* (1), 10−19.
(49) Ni, L.; Gallenkamp, C.; Paul, S.; Kübler, M.; Theis, P.; Chabbra, S.; Hofmann, K.; Bill, E.; Schnegg, A.; Albert, B.; Krewald, V.; Kramm, U. I. Active Site Identification in FeNC Catalysts and Their Assignment to the Oxygen Reduction Reaction Pathway by In Situ 57 Fe Mössbauer Spectroscopy. *Adv. Energy Sustainability Res.* **2021**, *2* (2), 2000064.
(50) Banham, D.; Ye, S.; Pei, K.; Ozaki, J.; Kishimoto, T.; Imashiro, Y. A review of the stability and durability of non-precious metal catalysts for the oxygen reduction reaction in proton exchange membrane fuel cells. *J. Power Sources* **2015**, *285*, 334−348.
(51) Kramm, U. I.; Zana, A.; Vosch, T.; Fiechter, S.; Arenz, M.; Schmeißer, D. On the structural composition and stability of Fe−N−C catalysts prepared by an intermediate acid leaching. *J. Solid State Electrochem.* **2016**, *20* (4), 969−981.
(52) Bates, J. S.; Martinez, J. J.; Hall, M. N.; Al-Omari, A. A.; Murphy, E.; Zeng, Y.; Luo, F.; Primbs, M.; Menga, D.; Bibent, N.; Sougrati, M. T.; Wagner, F. E.; Atanassov, P.; Wu, G.; Strasser, P.; Fellinger, T.-P.; Jaouen, F.; Root, T. W.; Stahl, S. S. Chemical Kinetic Method for Active-Site Quantification in Fe-N-C Catalysts and Correlation with Molecular Probe and Spectroscopic Site-Counting Methods. *J. Am. Chem. Soc.* **2023**, *145* (48), 26222−26237.
(53) Kramm, U. I.; Lefèvre, M.; Larouche, N.; Schmeisser, D.; Dodelet, J.-P. Correlations between mass activity and physicochemical properties of Fe/N/C catalysts for the ORR in PEM fuel cell via 57Fe Mössbauer spectroscopy and other techniques. *J. Am. Chem. Soc.* **2014**, *136* (3), 978−985.
(54) Ferrandon, M.; Kropf, A. J.; Myers, D. J.; Artyushkova, K.; Kramm, U.; Bogdanoff, P.; Wu, G.; Johnston, C. M.; Zelenay, P. Multitechnique Characterization of a Polyaniline−Iron−Carbon Oxygen Reduction Catalyst. *J. Phys. Chem. C* **2012**, *116* (30), 16001−16013.
(55) Kramm, U. I.; Herranz, J.; Larouche, N.; Arruda, T. M.; Lefèvre, M.; Jaouen, F.; Bogdanoff, P.; Fiechter, S.; Abs-Wurmbach, I.; Mukerjee, S.; Dodelet, J.-P. Structure of the catalytic sites in Fe/N/C-catalysts for O2-reduction in PEM fuel cells. *Phys. Chem. Chem. Phys.* **2012**, *14* (33), 11673−11688.
(56) Kishi, H.; Sakamoto, T.; Asazawa, K.; Yamaguchi, S.; Kato, T.; Zulevi, B.; Serov, A.; Artyushkova, K.; Atanassov, P.; Matsumura, D.; Tamura, K.; Nishihata, Y.; Tanaka, H. Structure of Active Sites of Fe-N-C Nano-Catalysts for Alkaline Exchange Membrane Fuel Cells. *Nanomaterials* **2018**, *8* (12), 965.
(57) Müller-Hülstede, J.; Schonvogel, D.; Schmies, H.; Wagner, P.; Dyck, A.; Wark, M. Incorporation of Activated Biomasses in Fe-N-C Catalysts for Oxygen Reduction Reaction with Enhanced Stability in Acidic Media. *ACS Appl. Energy Mater.* **2021**, *4* (7), 6912−6922.
(58) Uddin, A.; Dunsmore, L.; Zhang, H.; Hu, L.; Wu, G.; Litster, S. High Power Density Platinum Group Metal-free Cathodes for Polymer Electrolyte Fuel Cells. *ACS Appl. Mater. Interfaces* **2020**, *12* (2), 2216−2224.
(59) Jaouen, F.; Dodelet, J.-P. O 2 Reduction Mechanism on Non-Noble Metal Catalysts for PEM Fuel Cells. Part I: Experimental Rates of O 2 Electroreduction, H 2 O 2 Electroreduction, and H 2 O 2 Disproportionation. *J. Phys. Chem. C* **2009**, *113* (34), 15422−15432.
(60) Chen, J.; Yan, X.; Fu, C.; Feng, Y.; Lin, C.; Li, X.; Shen, S.; Ke, C.; Zhang, J. Insight into the Rapid Degradation Behavior of Nonprecious Metal Fe-N-C Electrocatalyst-Based Proton Exchange Membrane Fuel Cells. *ACS Appl. Mater. Interfaces* **2019**, *11* (41), 37779−37786.
(61) Kroschel, M.; Bonakdarpour, A.; Kwan, J. T. H.; Strasser, P.; Wilkinson, D. P. Analysis of oxygen evolving catalyst coated membranes with different current collectors using a new modified rotating disk electrode technique. *Electrochim. Acta* **2019**, *317*, 722−736.

https://doi.org/10.1021/acscatal.4c06338
ACS Catal. 2025, 15, 4477−4488

(62) Holst-Olesen, K.; Reda, M.; Hansen, H. A.; Vegge, T.; Arenz, M. Enhanced Oxygen Reduction Activity by Selective Anion Adsorption on Non-Precious-Metal Catalysts. *ACS Catal.* **2018**, *8* (8), 7104−7112.
(63) Müller-Hülstede, J.; Zierdt, T.; Schmies, H.; Schonvogel, D.; Meyer, Q.; Zhao, C.; Wagner, P.; Wark, M. Implementation of different Fe−N−C catalysts in high temperature proton exchange membrane fuel cells − Effect of catalyst and catalyst layer on performance. *J. Power Sources* **2022**, *537*, 231529.
(64) Zierdt, T.; Knake, J.; Müller-Hülstede, J.; Schonvogel, D.; Wagner, P.; Wark, M.; Friedrich, K. A. Effect of Non-ionic Surfactant on Fe-N-C Catalyst Layers under HT-PEMFC Conditions. *ECS Trans.* **2024**, *114* (5), 339−350.
(65) Zierdt, T.; Müller-Hülstede, J.; Schmies, H.; Schonvogel, D.; Wagner, P.; Friedrich, K. A. Effect of Polytetrafluorethylene Content in Fe-N-C-Based Catalyst Layers of Gas Diffusion Electrodes for HT-PEM Fuel Cell Applications. *ChemElectroChem* **2024**, *11* (5), No. e202300583.
(66) Osmieri, L.; Cullen, D. A.; Chung, H. T.; Ahluwalia, R. K.; Neyerlin, K. C. Durability evaluation of a Fe−N−C catalyst in polymer electrolyte fuel cell environment via accelerated stress tests. *Nano Energy* **2020**, *78*, 105209.

https://doi.org/10.1021/acscatal.4c06338
ACS Catal. 2025, 15, 4477−4488